



An Investigation of Disk Thickness in M51 from $H\alpha$, $P\alpha\alpha$, and Mid-infrared Power Spectra

Downloaded from: <https://research.chalmers.se>, 2025-06-24 08:32 UTC

Citation for the original published paper (version of record):

Calzetti, D., Adamo, A., Sandstrom, K. et al (2025). An Investigation of Disk Thickness in M51 from $H\alpha$, $P\alpha\alpha$, and Mid-infrared Power Spectra. *Astrophysical Journal*, 986(1).
<http://dx.doi.org/10.3847/1538-4357/adcee6>

N.B. When citing this work, cite the original published paper.



An Investigation of Disk Thickness in M51 from $H\alpha$, $Pa\alpha$, and Mid-infrared Power Spectra

Bruce G. Elmegreen¹, Daniela Calzetti², Angela Adamo³, Karin Sandstrom⁴, Daniel Dale⁵, Varun Bajaj⁶,
 Martha L. Boyer⁶, Ana Duarte-Cabral⁷, Ryan Chown⁸, Matteo Correnti^{9,10}, Julianne J. Dalcanton^{11,12},
 Bruce T. Draine¹³, Brandt Gaches^{14,15}, John S. Gallagher, III¹⁶, Kathryn Grasha^{17,18}, Benjamin Gregg²,
 Leslie K. Hunt¹⁹, Kelsey E. Johnson²⁰, Robert Kennicutt, Jr.^{21,22,23}, Ralf S. Klessen^{24,25,26,27,33}, Adam K. Leroy⁸,
 Sean Linden²³, Anna F. McLeod^{28,29}, Matteo Messa³⁰, Göran Östlin³, Mansi Padave⁴, Julia Roman-Duval⁶,
 J. D. Smith³¹, Fabian Walter³², and Tony D. Weinbeck⁵

¹ Katonah, NY 10536, USA

² Department of Astronomy, University of Massachusetts Amherst, 710 North Pleasant Street, Amherst, MA 01003, USA

³ Department of Astronomy, The Oskar Klein Centre, Stockholm University, AlbaNova, SE-10691 Stockholm, Sweden

⁴ Department of Astronomy & Astrophysics, University of California, San Diego, 9500 Gilman Drive, La Jolla, CA 92093, USA

⁵ Department of Physics and Astronomy, University of Wyoming, Laramie, WY 82071, USA

⁶ Space Telescope Science Institute, 3700 San Martin Drive, Baltimore, MD 21218, USA

⁷ School of Physics and Astronomy, Cardiff University, The Parade, Cardiff, CF24 3AA, UK

⁸ Department of Astronomy, The Ohio State University, 140 West 18th Avenue, Columbus, OH 43210, USA

⁹ INAF Osservatorio Astronomico di Roma, Via Frascati 33, 00078, Monteporzio Catone, Rome, Italy

¹⁰ ASI-Space Science Data Center, Via del Politecnico, I-00133, Rome, Italy

¹¹ Astronomy Department, University of Washington, Seattle, WA 98195, USA

¹² Center for Computational Astrophysics, Flatiron Institute, 162 Fifth Avenue, New York, NY 10010, USA

¹³ Department of Astrophysical Sciences, Princeton University, Princeton, NJ 08544, USA

¹⁴ Department of Space, Earth and Environment, Chalmers University of Technology, Gothenburg SE-412 96, Sweden

¹⁵ Faculty of Physics, University of Duisburg-Essen, Lotharstraße 1, 47057 Duisburg, Germany

¹⁶ Department of Astronomy, University of Wisconsin-Madison, 475 North Charter Street, Madison, WI 53706, USA

¹⁷ Research School of Astronomy and Astrophysics, Australian National University, Canberra, ACT 2611, Australia

¹⁸ ARC Centre of Excellence for All Sky Astrophysics in 3 Dimensions (ASTRO 3D), Australia

¹⁹ INAF—Osservatorio Astrofisico di Arcetri, Largo Enrico Fermi 5, 50125 Firenze, Italy

²⁰ Department of Astronomy, University of Virginia, Charlottesville, VA 22904, USA

²¹ Department of Physics and Astronomy, Texas A&M University, 578 University Drive, College Station, TX 77843, USA

²² George P. and Cynthia W. Mitchell Institute for Fundamental Physics & Astronomy, Texas A&M University, 578 University Drive, College Station, TX 77843, USA

²³ Department of Astronomy and Steward Observatory, University of Arizona, 933 North Cherry Avenue, Tucson, AZ 85721, USA

²⁴ Universität Heidelberg, Zentrum für Astronomie, Institut für Theoretische Astrophysik, Albert-Ueberle-Str. 2, 69120 Heidelberg, Germany

²⁵ Universität Heidelberg, Interdisziplinäres Zentrum für Wissenschaftliches Rechnen, Im Neuenheimer Feld 225, 69120 Heidelberg, Germany

²⁶ Harvard-Smithsonian Center for Astrophysics, 60 Garden Street, Cambridge, MA 02138, USA

²⁷ Radcliffe Institute for Advanced Studies at Harvard University, 10 Garden Street, Cambridge, MA 02138, USA

²⁸ Centre for Extragalactic Astronomy, Department of Physics, Durham University, South Road, Durham, DH1 3LE, UK

²⁹ Institute for Computational Cosmology, Department of Physics, Durham University, South Road, Durham, DH1 3LE, UK

³⁰ INAF-Osservatorio di Astrofisica e Scienza dello Spazio di Bologna, Via Gobetti 93/3, I-40129 Bologna, Italy

³¹ Ritter Astrophysical Research Center, University of Toledo, Toledo, OH 43606, USA

³² Max-Planck-Institut für Astronomie, Königstuhl 17, D-69117, Heidelberg, Germany

Received 2025 March 4; revised 2025 April 2; accepted 2025 April 5; published 2025 June 3

Abstract

Power spectra (PS) of high-resolution images of M51 (NGC 5194) taken with the Hubble Space Telescope and the James Webb Space Telescope (JWST) have been examined for evidence of disk thickness in the form of a change in slope between large scales, which map two-dimensional correlated structures, and small scales, which map three-dimensional correlated structures. Such a slope change is observed here in $H\alpha$, and possibly $Pa\alpha$, using average PS of azimuthal intensity scans that avoid bright peaks. The physical scale of the slope change occurs at ~ 120 pc and ~ 170 pc for these two transitions, respectively. A radial dependence in the shape of the $H\alpha$ PS also suggests that the length scale drops from ~ 180 pc at 5 kpc, to ~ 90 pc at 2 kpc, to ~ 25 pc in the central \sim kpc. We interpret these lengths as comparable to the thicknesses of the star-forming disk traced by H II regions. The corresponding emission measure is ~ 100 times larger than what is expected from the diffuse ionized gas. The PS of JWST Mid-IR Instrument images in eight passbands have more gradual changes in slope, making it difficult to determine a specific value of the thickness for this emission.

Unified Astronomy Thesaurus concepts: [Interstellar emissions \(840\)](#); [Spiral galaxies \(1560\)](#); [Interstellar dynamics \(839\)](#)

1. Introduction

The thickness of a face-on galaxy may be inferred from the Fourier transform power spectrum (PS) of turbulent gas, appearing as a transition where a shallow slope from two-dimensional structure on large scales changes to a steeper slope from three-dimensional structure on small scales

³³ Elizabeth S. and Richard M. Cashin Fellow.



(A. Lazarian & D. Pogosyan 2000). Numerical simulations (F. Bournaud et al. 2010; F. Combes et al. 2012; J. Fensch et al. 2023) illustrate this transition by showing large-scale velocities with two components in the plane of the disk, and small-scale velocities with three components inside the disk. PS breaks at the disk thickness have been observed previously for three galaxies: the Large Magellanic Cloud (LMC), M33, and NGC 1058. The LMC shows the PS break in H I (B. G. Elmegreen et al. 2001) and far-infrared dust emission (D. L. Block et al. 2010), with inferred disk thicknesses ranging from ~ 50 pc near 30 Dor and other bright H II regions, to ~ 250 pc in the central regions and ~ 400 pc in the outer regions (S. Szotkowski et al. 2019). In M33, the scale of the PS break ranges from ~ 50 pc in the far-ultraviolet and near-ultraviolet, to ~ 100 pc in H I and CO, to ~ 300 pc in H α , with the same full range also in the infrared (F. Combes et al. 2012). In NGC 1058, which is the furthest of these at a distance of ~ 10 Mpc, the transition was seen at 490 ± 90 pc in H I emission (P. Dutta et al. 2009).

The purpose of this paper is to report a fourth thickness measurement from PS, including an increase in thickness with radius, using $0''.07$ -resolution H α and Pa α images of M51 (2.54 pc FWHM at 7.5 Mpc, G. Csörnyei et al. 2023). We also examine the PS of the Mid-IR Instrument (MIRI) images of M51 at $0''.2$ – $0''.6$ resolution (7.3 pc–22 pc FWHM). Thickness is important for converting surface density into volume density for dynamical considerations (e.g., Q.-H. Peng 1988; C. Bacchini et al. 2020), correcting an observed rotation curve for radial pressure gradients to determine radial forces and the density of dark matter (R. Verbeke et al. 2017; P. E. Mancera Piña et al. 2022), and using it with the vertical velocity dispersion to determine the total disk mass (e.g., S. Sarkar & C. J. Jog 2018).

The thickness of M51 has been measured before. J. Pety et al. (2013) combined the Plateau de Bure interferometer and the IRAM 30 m telescope to infer that there are two molecular components, one with a scale height of 190–250 pc containing about half the ^{12}CO flux and another with a scale height of ~ 40 pc and an average density ~ 10 times higher. They also suggested that the H I in M51 has a similar two-tiered structure, based on a two-component fit to the average emission line profile. T. Hu et al. (2013) derived a stellar scale height of 95 pc–178 pc in M51 using the spiral arm pitch angle and density wave theory. R. G. Tress et al. (2020), who found a break in the PS of molecular gas at a scale of around 80 pc using numerical simulations of M51, provides a more direct comparison with our work.

The PS method for determining thickness is not always possible. E. W. Koch et al. (2020) examined the PS of mid- to far-infrared dust emission from the LMC, SMC, M31 and M33, and H I and CO emission from M31 and M33, finding no breaks other than what might result from bright point sources viewed through a point-spread function (PSF) and the exponential radial profile of the disk. We also saw a dominant influence of point sources and exponential profiles in B. G. Elmegreen et al. (2025, hereafter Paper I), which used mid-infrared James Webb Space Telescope (JWST) data to examine PS for NGC 628, NGC 5236, NGC 4449, and NGC 5068. We get around those problems here by using intensity scans in the azimuthal direction and selecting only scans without strong point sources.

Observations of other galaxies, usually with H I, do not generally have high enough spatial resolution to see a break in

the PS from disk thickness. P. Dutta et al. (2010) measured a PS slope of -1.7 for NGC 4254, but could only observe scales larger than 1.7 kpc. In a second study, P. Dutta et al. (2013) measured slopes averaging -1.3 for 18 other spirals, but for scales larger than the likely thicknesses. The H I column density in NGC 6946 has a PS slope of -0.96 ± 0.05 determined by M. Nandakumar & P. Dutta (2023) down to ~ 150 pc. K. Grisdale et al. (2017) measured PS of the H I surface densities for six THINGS galaxies, finding large-scale slopes of -2.2 for NGC 628, -2.8 for NGC 3521, -2.1 for NGC 4736, -2.2 for NGC 5055, -2.5 for NGC 5457, and -1.6 for NGC 6946. All of these PS are for two-dimensional maps. The PS determined here are from one-dimensional intensity scans, which are used to avoid bright point-like sources. The PS slope for a one-dimensional scan should be shallower by 1 than the slope for a two-dimensional scan.

For the PS method to work, the physical scale of the thickness has to be resolved by at least a factor of ~ 10 , and the thickness has to be smaller than the whole galaxy by another factor of ~ 10 , in order to determine power-law slopes on either side of the PS break. This dual constraint is satisfied for H I and far-infrared observations of the angular-largest galaxies in the Local Group (the LMC and M33), and it is satisfied by ground-based, optical observations of large galaxies out to ~ 3 Mpc, such as M81 (B. G. Elmegreen et al. 2003), but more distant spirals are expected to have disks that are too thin in angle to resolve in the first constraint, and nearby dwarfs, including the SMC (S. Szotkowski et al. 2019), are probably too thick to satisfy the second constraint (e.g., N. N. Patra 2020a). A third constraint is that the emission has to come from spatially correlated structures so the PS is a power law and not, for example, flat on a log-log plot from noise. Such correlated structure was an early discovery for H I gas (J. Crovisier & J. M. Dickey 1983), showing that it is highly turbulent (see also J. W. Armstrong et al. 1995; B. G. Elmegreen & J. Scalo 2004).

The thickness of a gas disk can also be measured using theoretical considerations of vertical equilibrium (e.g., L. Spitzer 1942; E. N. Parker 1966; P. C. van der Kruit 1981; C. A. Narayan & C. J. Jog 2002; H. Koyama & E. C. Ostriker 2009; E. C. Ostriker et al. 2010). This requires, for the upward component of force, observations of the gas velocity dispersion combined with estimates of magnetic and cosmic ray pressures, and, for the downward force, observations of the total mass surface density from gas, stars, and dark matter inside the gas disk, along with the vertical component of forces from the bulge and dark matter halo (e.g., P. Girichidis et al. 2016; A. S. Hill et al. 2018; C. D. Wilson et al. 2019).

The equilibrium method has been applied to the H I layers of many galaxies, including the Milky Way (P. M. W. Kalberla et al. 2007; A. Banerjee & C. J. Jog 2011) and outer parts of M31 (A. Banerjee & C. J. Jog 2008), 20 galaxies in I. Bagetakos et al. (2011), four dwarf irregulars in A. Banerjee et al. (2011), superthin galaxies in A. Banerjee et al. (2010) and A. Banerjee & C. J. Jog (2013), 20 dwarf irregulars in B. G. Elmegreen & D. A. Hunter (2015), seven spirals and 23 dwarfs in N. N. Patra (2020b) and N. N. Patra (2020a), 10 dwarf irregulars in C. Bacchini et al. (2020), 28 H I-rich galaxies and 26 comparison galaxies in T. H. Randriamampandry et al. (2021), and an ultradiffuse galaxy plus 14 dwarf irregulars in X. Li et al. (2022). Disk thicknesses for H I typically exceed several hundred parsecs. C. Bacchini et al. (2019) determined H I and molecular thicknesses in 12 spirals, P. E. Mancera Piña et al. (2022)

determined them for 32 dwarfs and spirals, while for the molecular component alone, N. N. Patra (2019) measured eight spirals, C. D. Wilson et al. (2019) five ultra-luminous infrared galaxies, and J. Molina et al. (2020) two starburst galaxies at redshift $z \sim 0.15$. For NGC 6946, N. N. Patra (2021) used the equilibrium method for a multicomponent disk to compare model CO line profiles with observed profiles and found that two molecular components fit best: one thin, with 30% of the emission and a half-width at half-maximum (HWHM) of ~ 50 pc at 4 kpc radius, and the other twice as thick and coincident with the HI disk.

Edge-on galaxies, including the Milky Way, have had their thicknesses measured directly. The HWHM of the molecular cloud layer in the Milky Way is ~ 50 pc inside the solar circle (M. Heyer & T. M. Dame 2015). This is determined mostly by the dense molecular gas detected in both ^{12}CO and ^{13}CO , while the diffuse CO, detected only in ^{12}CO , is $\sim 50\%$ thicker (J. Roman-Duval et al. 2016). Numerical simulations of the Milky Way by S. M. R. Jeffreson et al. (2022) obtained a similar ~ 50 pc HWHM. NGC 891 has a CO HWHM of 110 pc (N. Z. Scoville et al. 1993) to 160 pc (K. Yim et al. 2011), which is consistent with the HWHM of 105 pc for 133 $8\ \mu\text{m}$ star-forming cores in that galaxy (B. G. Elmegreen & D. M. Elmegreen 2020). NGC 891 also has a much wider layer of diffuse ionized gas (DIG) with a scale height of ~ 1 kpc (R. J. Dettmar 1990; R. J. Rand et al. 1990), composed of nearly vertical filaments (J. C. Howk & B. D. Savage 2000; J. Rossa et al. 2004). A CO counterpart to the thick disk in NGC 891 was suggested by S. Garcia-Burillo et al. (1992) but not seen by K. Yim et al. (2011), although K. Yim et al. (2011) measured the HWHM of HI to be 435 pc for a single component fit and 325 pc and 1 kpc for a two-component fit. N. N. Patra (2018) derived an equilibrium HWHM of 50 pc to 80 pc at 6 kpc radius for molecules in the edge-on galaxy NGC 7331. HI in the edge-on dwarf irregular KK250 has a HWHM of 350 pc (N. N. Patra et al. 2014), and HI in the spiral IC 2233 has a HWHM of 500 pc (L. D. Matthews & J. M. Uson 2008). In NGC 4157, NGC 4565, and NGC 5907, K. Yim et al. (2014) measured disk thicknesses as a function of radius for CO and HI; at 4 kpc radius, their linear fits imply HWHM of 120 pc, 45 pc, and 50 pc for CO and 450 pc, 180 pc, and 400 pc for HI, respectively (converting from their Gaussian widths to HWHM).

Whenever it can be observed, disk thickness increases with radius, although not exponentially as it would for a constant velocity dispersion and exponentially decreasing surface density. Vertical velocity dispersions tend to decrease with radius (D. Tamburro et al. 2009), making the thickness increase more linearly (e.g., K. Yim et al. 2011, 2014; B. G. Elmegreen & D. M. Elmegreen 2020; N. N. Patra 2020b).

The organization of this paper is as follows: Section 2 summarizes the $\text{H}\alpha$, $\text{Pa}\alpha$, and broadband data used here, Sections 3–5 show the PS for $\text{H}\alpha$, $\text{Pa}\alpha$, and eight mid-infrared bands, Section 6 contains a discussion, and Section 7 has our conclusions.

2. Data

The Hubble Space Telescope (HST) wide field camera (WFC) optical imaging of M51 for $\text{H}\alpha$ was obtained by GO-10452 (PI: S. Beckwith), as part of the HST image release program by the Hubble Heritage Team. The imaging is a 2×3 mosaic covering the bright area of M51 and its companion

NGC 5195. Observations in F555W, F658N, and F814W filters were retrieved from the MAST Archive,³⁴ reduced, and aligned to the Gaia reference system. The final pixel scale of the drizzled HST mosaics is $0''.04\ \text{px}^{-1}$. Flux calibration is in units of counts s^{-1} , which were converted to physical units using the PHOTFLAM image header keywords.

JWST near-IR imaging with NIRCcam for $\text{Pa}\alpha$ was obtained via the Cycle 1 JWST program #1783 (Feedback in Emerging extragalactic Star clusters, JWST-FEAST, PI: A. Adamo). For this work, we only utilize the F150W, F187N, and F200W filter mosaics. The NIRCcam mosaics were processed through the JWST pipeline version 1.12.5 (2023 December release) using the Calibration Reference Data System (CRDS) context “jwst 1174.pmap.”³⁵ The NIRCcam mosaics have been aligned to the Gaia reference system with a common pixel scale of $0''.04$, and are in units of janskys per pixel ($\text{Jy}\ \text{px}^{-1}$).

The NIRCcam F187N centered on the $\text{Pa}\alpha$ line emission ($\lambda = 1.8789\ \mu\text{m}$ at the fiducial redshift $z = 0.00174$)³⁶ and the ACS/WFC F658N centered on the $\text{H}\alpha + [\text{N II}]$ doublet line emission ($\lambda = 0.6559\ \mu\text{m}$, $0.6574\ \mu\text{m}$, $0.6595\ \mu\text{m}$ at $z = 0.00174$ (see footnote 34)), were used to derive emission line maps. The stellar continuum image for the F187N was derived by interpolating between F150W and F200W. As the F200W contains the $\text{Pa}\alpha$ emission, we iteratively subtracted the line from this filter, using the procedure described in M. Messa et al. (2021), B. Gregg et al. (2024), and D. Calzetti et al. (2024), until differences between two subsequent iterations are $\leq 0.1\%$ in flux. The stellar continuum image to subtract from the F658N filter was derived by interpolating between F555W and F814W. F555W includes the $[\text{O III}](\lambda 0.5007\ \mu\text{m})$ line emission, but D. Calzetti et al. (2024) showed that in metal-rich galaxies this contribution is small, affecting the stellar continuum by $\leq 1.5\%$.

The 3σ detection limits for the emission lines were derived after converting the line maps into physical flux maps. The F658N map used here, which includes the $\text{H}\alpha$ and $[\text{N II}]$ emission lines, were multiplied by the filter width of $0.0087\ \mu\text{m}$ after the continuum was subtracted.³⁷ The F187N map, which contains the $\text{Pa}\alpha$ emission line, was multiplied by its filter width of $0.024\ \mu\text{m}$ (see footnote 35) after continuum subtraction. Both were corrected for the filter transmission curve value at the galaxy’s redshift. The resulting 3σ detection limits are then $7.7 \times 10^{-17}\ \text{erg}\ \text{s}^{-1}\ \text{cm}^{-2}\ \text{arcsec}^{-2}$ for $\text{H}\alpha$ (including $[\text{N II}]$ emission) and $3.8 \times 10^{-17}\ \text{erg}\ \text{s}^{-1}\ \text{cm}^{-2}\ \text{arcsec}^{-2}$ for $\text{Pa}\alpha$.

JWST MIRI mosaics of M51 were obtained as part of both the Cycle 1 FEAST program and the Cycle 2 M51 Treasury program #3435 (The JWST Whirlpool Galaxy Treasury, PI: K. Sandstrom & D. Dale). The FEAST program obtained mosaics in the F560W and F770W filters aiming to maximize overlap with the NIRCcam mosaics, while the M51 Treasury obtained mosaics in the F1000W, F1130W, F1280W, F1500W, F1800W, and F2100W matching the FEAST observing strategy. Both programs used a 1×5 pointing mosaic to cover $\sim 12\ \text{arcmin}^2$ of M51’s disk. The observations used a four-point dither cycling dither pattern. The MIRI mosaics were processed

³⁴ The Mikulski Archive for Space Telescopes at the Space Telescope Science Institute: <https://archive.stsci.edu/>.

³⁵ https://jwst-pipeline.readthedocs.io/en/latest/jwst/user_documentation/reference_files_crds.html

³⁶ From NED, the NASA Extragalactic Database.

³⁷ https://etc.stsci.edu/etcstatic/users_guide/appendix_b_acs.html; <https://jwst-docs.stsci.edu/jwst-near-infrared-camera/nircam-instrumentation/nircam-filters>

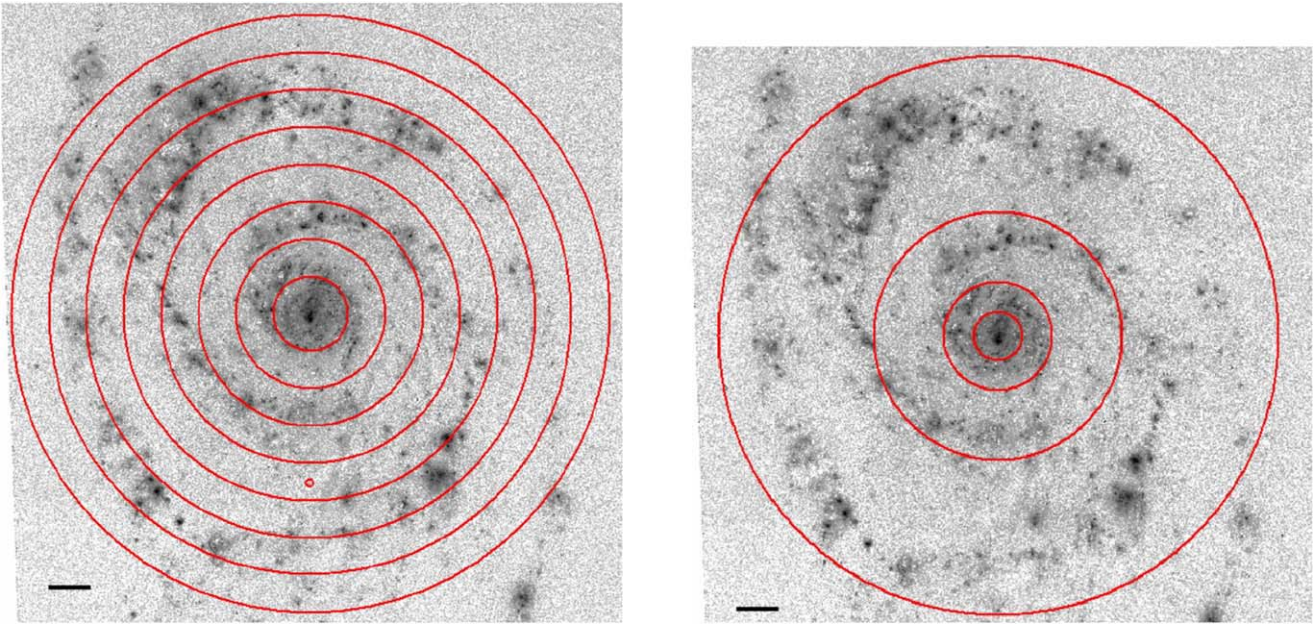


Figure 1. Left: image of M51 in H α with concentric circles at sample radii of azimuthal intensity scans used to derive the PS. The circles are spaced by 600 pixels, which is 200 scans, $24''$, or 872 pc. A small circle midway between the fourth and fifth annuli below the center has a diameter corresponding to 200 pc. Right: H α with circles at $16''$, $35''$, $80''$, and $180''$ used to determine the radial intervals for separate evaluations of thickness. The images are plotted as log of the intensity. The scale bar indicates 1 kpc.

through the JWST pipeline version 1.13.4 (Feb 2024 release) using the CRDS context “jwst 1241.pmap” (see footnote 33); these mosaics have a pixel scale of $0''.11$ and are in units of megajanskys per steradian (MJy sr $^{-1}$).

3. Power Spectra for H α Emission

The radial profile of intensity from the exponential disk of M51 contributes to the two-dimensional PS on large scales (Paper I). To avoid that component here, PS were determined from azimuthal intensity scans. The PS of an azimuthal scan is not exactly the same as the PS of a straight-line scan because the slight curvature of the arc inside each azimuthal pixel distorts the wavenumber scale by a small amount. The difference is unimportant if the circumference is large compared to the PS features of interest. Here, we highlight ≤ 200 pc scales, which correspond to less than $5''.5$ or 138 pixels, which is much smaller than the circumference scan lengths ($\sim 15,000$ pixels at midradius). We avoid unnecessary pixel interpolation by using projected circles rather than deprojected circles in the plane of the disk. This approximation is acceptable because the 20° inclination of M51 (T. Hu et al. 2013) is small, so the line-of-sight thickness increases with the tilt by only $1/\cos 20^\circ = 1.06$. Also, it affects mostly the $k=2$ component of the PS by foreshortening the pixels on the major axis compared to the minor axis, and by sampling slightly different galactocentric radii on the two axes. These two effects amount to $\leq 10\%$ error at $k \sim 2$. This is far from the wavenumber range of interest, which is larger by the ratio of the diameter of the galaxy to the thickness, a factor of ~ 100 .

Figure 1 shows the positions of eight circular scans on the H α image, separated uniformly by 600 pixels (872 pc). We measured the intensity in 1623 such circles, one pixel wide and separated by 3 pixels to avoid overlaps. Figure 1 shows every 200th scan. For comparison, a length of 200 pc corresponds to the diameter of the tiny circle between the fourth and fifth large

circles below the center; it is very small on this image. The black line in the lower left corresponds to 1 kpc. Most of the obvious features in the figure are larger than the disk thickness derived in this paper.

Figure 2 plots the distribution function of pixel values (left) and peak values for each scan (right). As noted above, the 3σ detection for H α is 7.7×10^{-17} erg s $^{-1}$ cm $^{-2}$ arcsec $^{-2}$, which is $10^{-3.1}$ on the x-axis in Figure 2 (red dashed line). This noise limit corresponds to the maximum in the pixel intensity distribution in the left-hand panel, so the histogram at smaller values is dominated by noise. The peak intensity distribution in the right-hand panel is significantly above the noise limit.

Figure 3 shows intensity scans at the top and their PS at the bottom. Those on the left are a selection of scans approximately corresponding to the eight circles in Figure 1, increasing in length as the circle circumference increases. Some of these scans have single bright sources that distort the PS, as shown in the lower left. For example, the second and third scans up from the bottom have bright H α sources at pixel values of 4061 and 3397, respectively; the ordinate scales are compressed by factors of 2 and 20 to show these scans in the figure. The corresponding PS of these scans are relatively flat in the lower panel. To avoid including these distorted PS in radial averages, we concentrated on scans with no bright peaks, as shown in the right-hand panels. In the top right are intensity scans close in radius to those on the left (as evident from the comparable scan lengths) but without bright peaks. Note that the ordinate stretch is larger by a factor of 10 in the top right, and that 3σ for H α corresponds to 0.00077 on both ordinates. The intensity scans in the top right have their PS in the bottom right; they are relatively similar and suitable for averaging. In what follows, we avoid H α intensity scans with peaks brighter than certain limits, which range between 0.108 and 0.324 in the units of the ordinate in the top plots, which is 10^{-13} erg s $^{-1}$ cm $^{-2}$ arcsec $^{-2}$.

The PS at the bottom of Figure 3 plot wavenumber k (inverse of length) on the abscissa, normalized to the wavenumber k_0

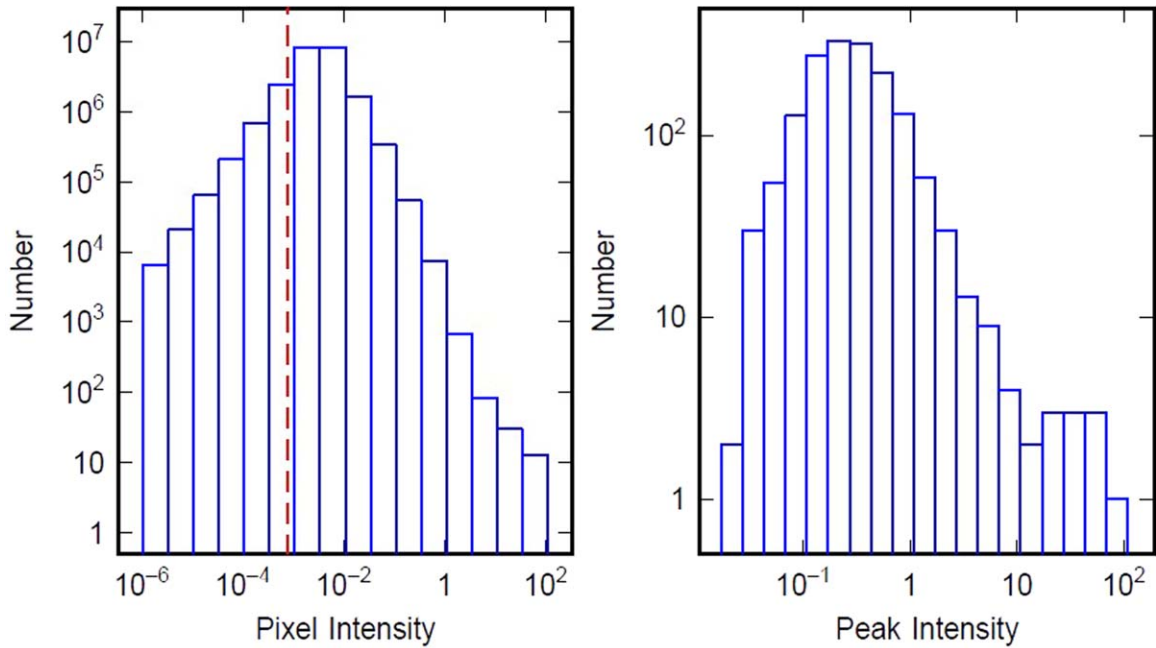


Figure 2. Histograms of pixel $H\alpha$ intensity values (in units of $10^{-13} \text{ erg s}^{-1} \text{ cm}^{-2} \text{ arcsec}^{-2}$, left) and peak intensities in each scan (right). The peak intensity upper cutoffs used to select scans without strong sources are 0.108, 0.162, 0.216, and 0.324 in these units. These values on the abscissa of the right-hand histogram give an indication of how many scans had to be removed (i.e., those with higher peak values) to see the break in the $H\alpha$ PS. The vertical dashed line on the left-hand histogram is the 3σ noise level.

corresponding to an inverse length of 2 pixels (i.e., the number of 2 pixel wavelengths that fit in the intensity strip is k_0). This normalization is convenient because it does not depend on angular resolution through the PSF, which shows up as the width of the dip at high k/k_0 , or source distance, which comes in as a coordinate conversion from k/k_0 to parsecs, shown on the top axis. The PS themselves are calculated from the sum of the squares of the sine and cosine Fourier transforms using angle $2\pi kx/L$ for position x from 1 to the scan length L in pixels, and k from 1 to $L/2$. The number of k/k_0 values is half the number of pixels in the scan length, and the wavelength is 2 pixels divided by k/k_0 . The PS extend to lower k/k_0 values as the scan length increases. The absolute normalization of the PS on the ordinate of Figure 3 is arbitrary; they are shifted vertically for clarity. The relative scale indicated by the tick marks is accurate, so the PS slopes may be read directly from the figure using these axes.

Figure 4 shows PS (top) and their running derivatives (bottom) for $H\alpha$ (left), $\text{Pa}\alpha$ (middle; discussed in Section 4) and mid-infrared passbands (right, discussed in Section 5). The PS are averaged over the radial ranges indicated. The averages were made by interpolating all the individual PS, $P_i(k_i/k_{0,i})$, into values where their relative wavenumbers, $k_i/k_{0,i}$, equal the relative wavenumbers of the longest PS, $P_{\text{long}}(k_{\text{long}}/k_{0,\text{long}})$, i.e., where $k_i = k_{\text{long}}(k_{0,i}/k_{0,\text{long}})$. This interpolation ensures averaging at the same physical scales, tied to pixel size. The longest PS is the one from the scan with the largest radius in the average.

The running slopes of the average PS in the bottom panels of Figure 4 were determined by dividing the range of k/k_0 into 50 equal intervals of $\log k/k_0$ and evaluating the average of the logarithm of the average PS in each interval and the average of the $\log(k/k_0)$ values in each interval. The running slope is the ratio of the difference between the interval-averaged \log -PS at locally higher and lower k/k_0 to the difference between the interval-averaged $\log(k/k_0)$ at these higher and lower k/k_0 . This procedure of dividing the wavenumbers into equal log

intervals was done because the density of PS values on the $\log k/k_0$ axis is not constant. The black horizontal lines superposed on the running slopes are least-squares fits over intervals of wavenumber that are discussed below. The zero levels for the slopes are indicated by circles.

We consider the results for $H\alpha$ first. In order to select scans without strong sources and test the robustness of the results against the specific choice of an intensity cutoff, we experimented with four values that gave various numbers of PS in the average. From top to bottom in the left-hand panels of Figure 4, the first four PS and their corresponding derivatives exclude scans with peaks exceeding 1.08, 1.62, 2.16, and 3.24 in units of $10^{-14} \text{ erg s}^{-1} \text{ cm}^{-2} \text{ arcsec}^{-2}$. They also exclude scans with negative peaks, which arise from the continuum subtraction (negative intensity peaks make the same PS distortions as positive peaks). Because of these cutoffs, the top PS includes the fewest scans in the average (197 scans out of 1623 total) and has the smallest distortions from bright point sources. The fourth PS from the top includes 710 scans with slightly brighter intensity peaks. The bottom PS includes all the scans without negative peaks, even if they have large positive peaks (1130 scans). The PS most representative of the faintest emission are the top few. Large fluctuations at low k/k_0 are partly from noise and a low density of values there on the logarithmic axis.

In the top-left panel of Figure 4, in cyan, is an example of a PS with a bright pixel at $13^{\text{h}}29^{\text{m}}45^{\text{s}}.97$, $47^{\circ}11'20''.56$. This pixel may be an image flaw, but the scan is treated like the others so it shows the PS of the PSF along a one-dimensional scan. The PS is flat at low k/k_0 and dips down at high k/k_0 where the PSF removes finer-scale structure.

The top three PS in the top-left panel of Figure 4 have slight breaks at a size scale of $1/k \sim 120 \text{ pc}$, which is shown by the vertical black line (as discussed in the next paragraph). The running slopes in the bottom panel show a corresponding jump at $\sim 120 \text{ pc}$, with approximately constant values on either side.

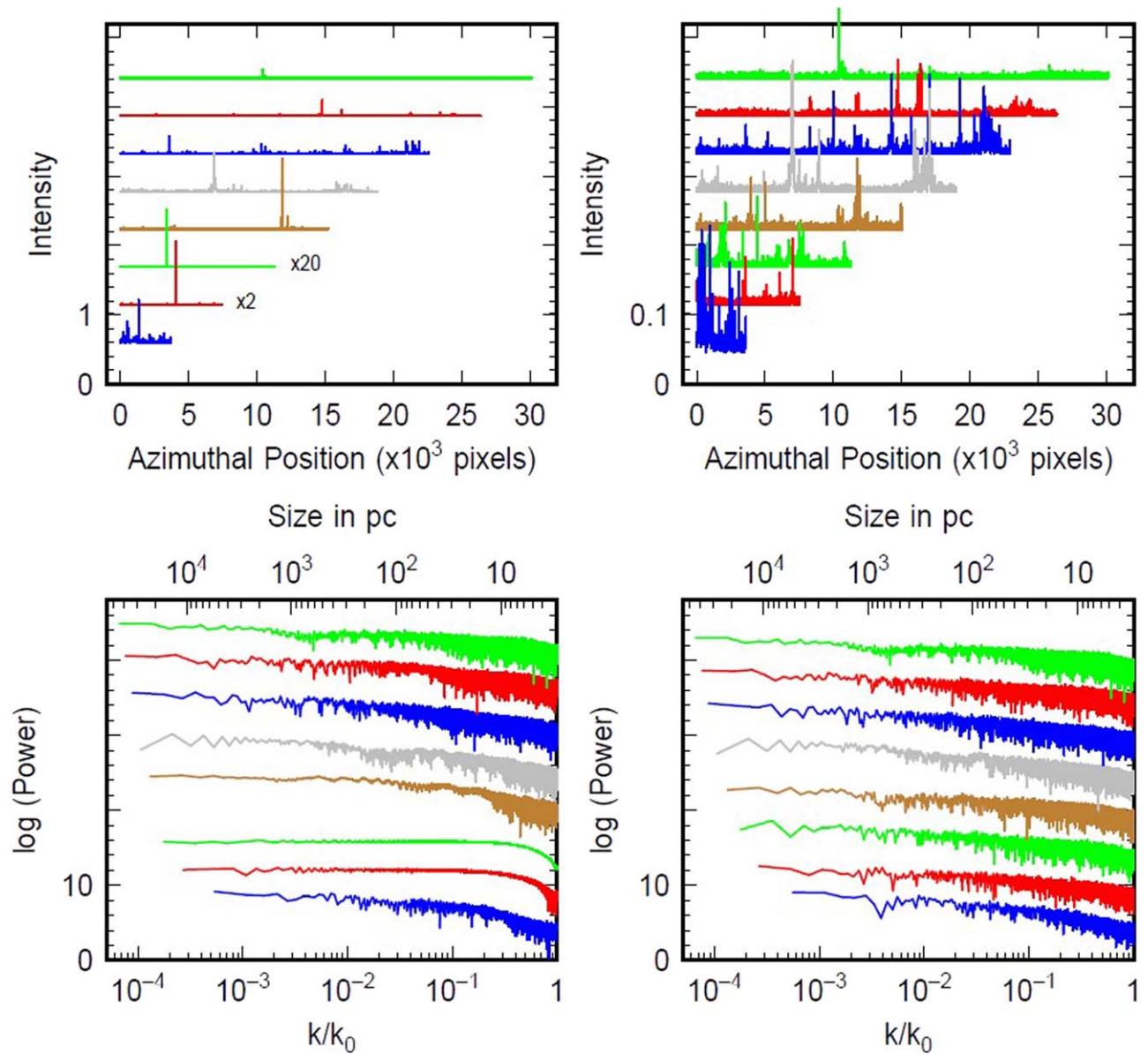


Figure 3. Left: $H\alpha$ intensity scans (with the indicated interval in units of $10^{-13} \text{ erg s}^{-1} \text{ cm}^{-2} \text{ arcsec}^{-2}$, top) and PS (in the square of these units, bottom) corresponding approximately to the positions of the circles in Figure 1. Both are shifted vertically by arbitrary amounts for clarity. The intensity ordinate is a linear scale with one unit shown; factors of 2 and 20 compressions are used for the second and third scans up from the bottom. The PS ordinate shows the 10 unit scale, which means the PS covers a range of 10^{10} in that interval. The lengths of the scans increase with radius. Right: intensity scans (top) and PS (bottom) also corresponding to radii near the circles in Figure 1, but chosen to avoid strong sources. The PS in the lower left are irregular. For example, they are flat at low $\log k/k_0$ when there are exceptionally strong sources in the scans. When there are no strong sources, the PS (lower right) are more uniform and may be averaged to give a better composite PS.

The black horizontal lines at low k/k_0 are least-squares fits to the PS slopes between $k=1$ and the value of k/k_0 corresponding to 120 pc. The black line at large k/k_0 is the least-squares fit to the slope between 120 pc and the value of k/k_0 at 5 times the FWHM of the PSF; this FWHM for $H\alpha$ is $0''.07$, or 2.55 pc. The intensity limits and numbers of scans included in each PS average, and the slopes for low and high k/k_0 parts of the PS averages, are in Table 1. Slope errors in the table are the 90% uncertainty limits in a Student t-distribution. The lowest PS among the five averages shown, which was made from the most intensity scans, has a continuously varying slope because it is a superposition of PS with different shapes (Figure 3).

We measured the break scale of ~ 120 pc from the k/k_0 value at the intersection between the power-law fits above and below

a first break-scale estimate (~ 100 pc). These power-law fits typically included a wide k/k_0 range and did not vary significantly if the range changed slightly. To determine the uncertainty of the break scale, we measured the rms deviation between the power-law fit and the PS on each side of the break estimate, and then found the values of k/k_0 above and below the fitted break where the power law equaled the break value minus and plus, respectively, the rms deviations. The physical scales corresponding to these k/k_0 and their uncertainties are in Table 1; 120 pc is an approximate average for these.

The $H\alpha$ PS also suggest that the disk thickness increases with galactocentric radius. Figure 5 shows three columns of average PS and their running slopes in radial intervals from $16''$ to $35''$ (0.58 kpc–1.27 kpc) on the left, $35''$ to $80''$ (1.27 kpc–

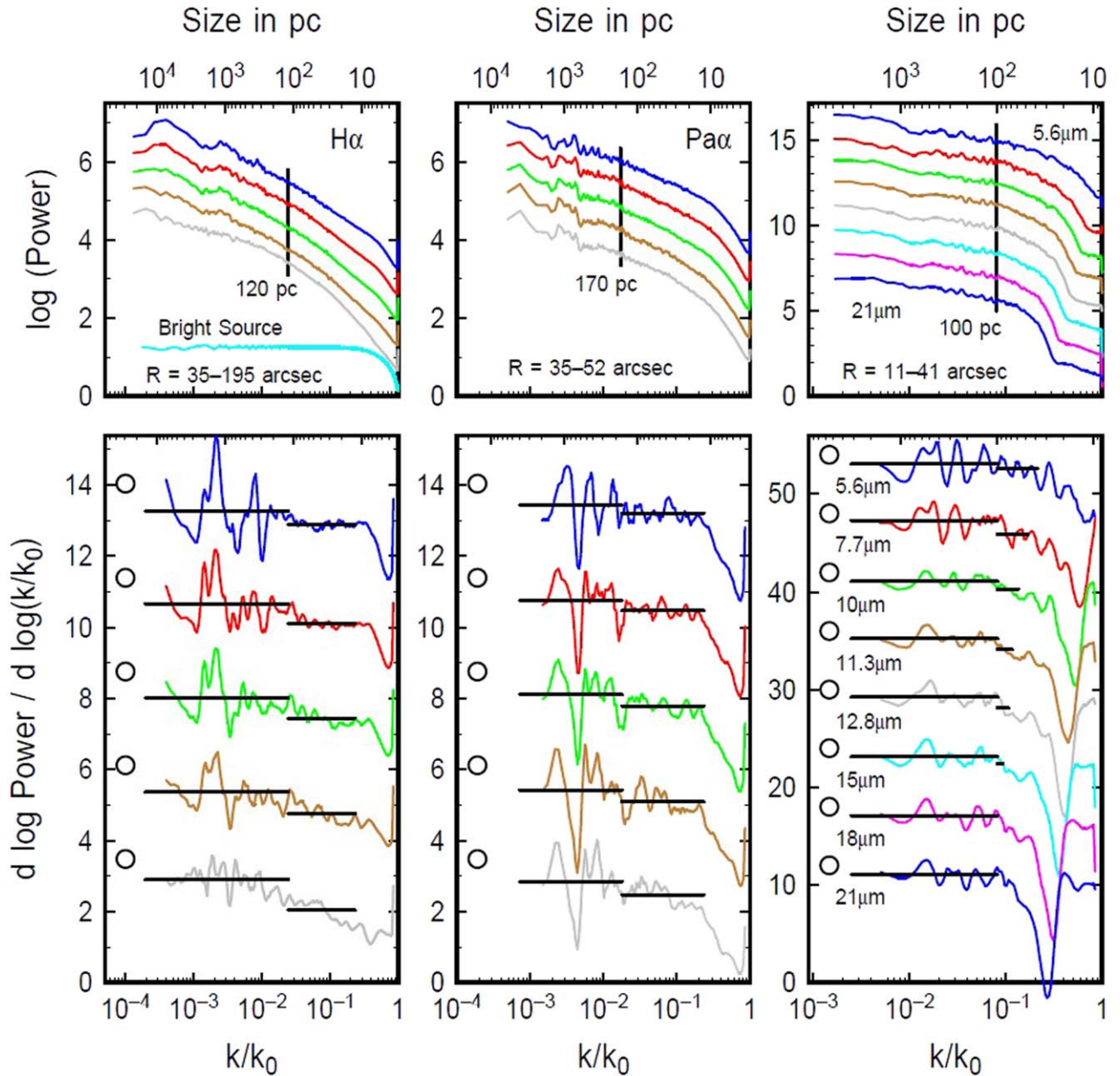


Figure 4. PS (top) and their running slopes (bottom) for H α (left), Pa α (middle), and eight mid-infrared passbands (right). The curves are shifted upward for clarity with slope zero levels in the bottom panels indicated by circles. For H α and Pa α , the top curves in each panel have the lowest intensity limits and the smallest numbers of scans in the average PS, and the bottom curves in each panel have all the scans, excluding only those with negative intensity peaks. The eight PS on the right correspond to the eight near-infrared bands, as labeled in the bottom panel; each is from an average of the PS with the lowest intensity peaks. A slight break at a size of $1/k \sim 120$ pc is visible in the top three H α PS (at the vertical black line). A weaker break at ~ 170 pc is in some of the Pa α PS. The mid-infrared PS on the right have a more gradual change in slope; there is no obvious break but a vertical line shows 100 pc. The running slopes in the bottom panels show sudden changes at the positions of the PS breaks. The horizontal black lines are least-squares fits to the PS slopes at wavenumbers below the suggested breaks and at wavenumbers above the breaks and up to the value of k/k_0 corresponding to 5 times the FWHM of the PSF. The mid-infrared passbands on the right have little or no span of PS from the fiducial scale of 100 pc to the PSF. The cyan curve in the top-left panel is the PS of an H α intensity scan with a bright point-like source. Radial ranges for the PS are indicated in the top panel.

2.91 kpc) in the middle, and $80''$ to $180''$ (2.91 kpc–6.54 kpc) on the right. These interval limits are shown as circles on the right-hand side of Figure 1. As in Figure 4, the numbers of scans in the average PS increase from top to bottom with a sequence of increasing cutoff values (Table 2). For the mid- and large radial intervals, the cutoff sequence is the same as for H α in Figure 4, but for the lowest radial range, the cutoff values are twice as large to get enough scans in the average.

The breaks in the PS change with radius, increasing from ~ 25 pc at $R < 35''$, to ~ 90 pc at midradius, and to ~ 180 pc at the larger radii (Table 2). The running slopes in the bottom

panels show corresponding shifts. The scale of the PS break at the smallest radius is comparable to 5 times the FWHM of the PSF, which is the limit of our capability, so the thickness there could be smaller than 25 pc.

4. Power Spectrum for Pa α Emission

Azimuthal scans were also taken for Pa α , using data from JWST (Section 2). The Pa α image with representative circles for the scans is shown in Figure 6. As for H α , the pixel size is 0.04 and the scans are taken every 3 pixels. The figure shows

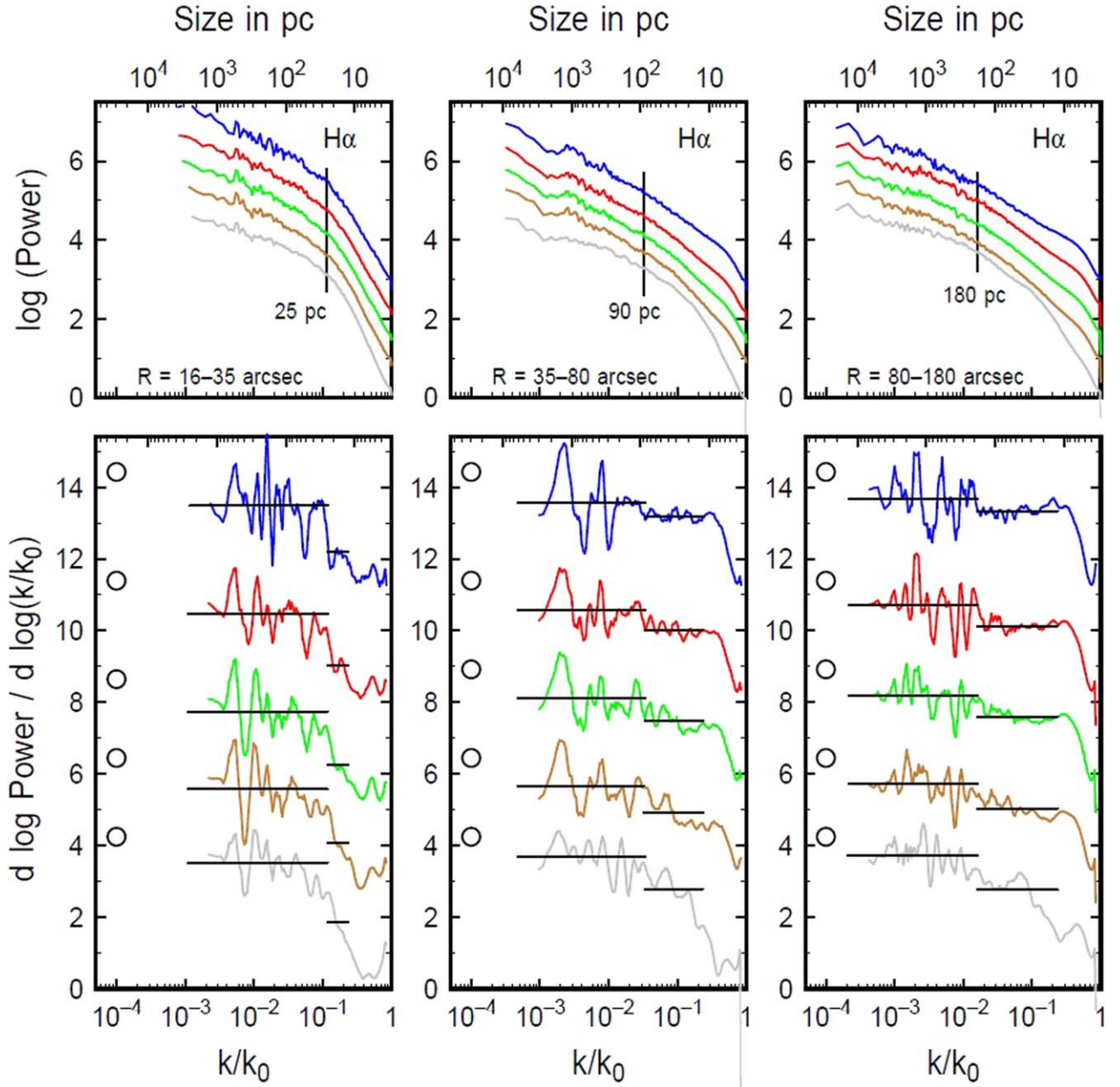


Figure 5. Average PS (top) and their running slopes (bottom) are shown for three indicated intervals of galactocentric radius (left to right). As for the H α in Figure 4, the peak intensities and the number of PS in the averages both increase from the top curve to the bottom curve, showing the tendency for the PS break to appear only when the weakest intensities are considered. There is a clear change in PS shape as the length scale corresponding to the PS break increases with radius. Zero levels for the running slopes are indicated by circles.

Table 1
PS Results for H α at Various Peak Intensity Thresholds

Threshold ^a	0.108	0.162	0.216	0.324	None
Number of scans	197	375	508	710	1130
Slope, low k/k_0	-0.77 ± 0.04	-0.73 ± 0.03	-0.75 ± 0.03	-0.76 ± 0.02	-0.58 ± 0.02
Slope, high k/k_0	-1.17 ± 0.01	-1.28 ± 0.02	-1.32 ± 0.03	-1.36 ± 0.03	-1.45 ± 0.03
Break scale (pc) ^b	148^{30}_{17}	118^{20}_{10}	114^{18}_9	113^{17}_9	126^{35}_{12}

Notes.

^a Peak intensity threshold in units of $10^{-13} \text{ erg s}^{-1} \text{ cm}^{-2} \text{ arcsec}^{-2}$.

^b Break scales are from the intersection points of the power-law fits to the PS on scales larger and smaller than ~ 100 pc. The slopes of the PS are from fits at k/k_0 smaller than and larger than 120 pc, which is about the average of the tabulated break scales.

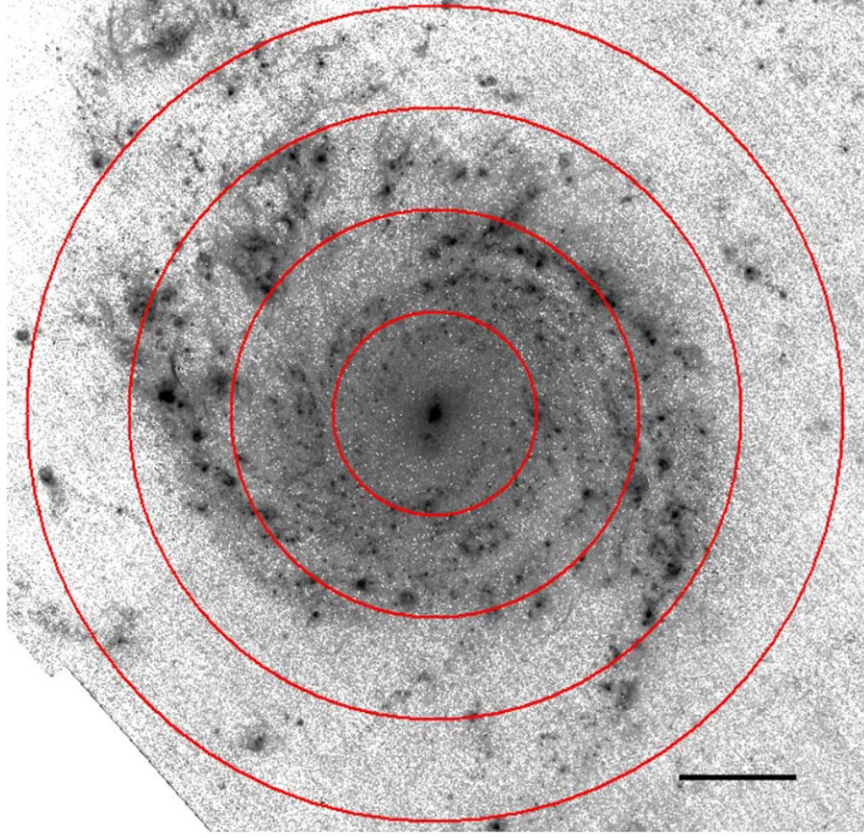


Figure 6. The Pa α image of M51 is shown with circles corresponding to scan positions separated by 300 pixels, which is 100 scans, 12'', and 436 pc. The image is plotted as log of the intensity. This part of the galaxy surveyed at Pa α is about one-quarter the size of the H α image in Figure 1. The scale bar is 500 pc.

Table 2
PS Results for H α at Various Radii

16'' to 35'' (0.58–1.27 kpc)					
Threshold ^a	0.216	0.324	0.432	0.648	none
Number of scans	21	51	73	102	128
Low k/k_0	-0.97 ± 0.04	-0.96 ± 0.03	-0.95 ± 0.04	-0.91 ± 0.04	-0.77 ± 0.03
High k/k_0	-2.24 ± 0.34	-2.35 ± 0.18	-2.53 ± 0.16	-2.60 ± 0.15	-2.71 ± 0.11
Break scale ^b	$29.3^{7.0}_{2.6}$	$28.3^{6.5}_{2.3}$	$26.5^{6.0}_{2.0}$	$25.7^{5.8}_{1.8}$	$25.7^{8.8}_{2.1}$
35'' to 80'' (1.27–2.91 kpc)					
Threshold ^a	0.108	0.162	0.216	0.324	none
Number of scans	76	143	187	239	347
Low k/k_0	-0.87 ± 0.04	-0.82 ± 0.04	-0.81 ± 0.04	-0.79 ± 0.04	-0.57 ± 0.03
High k/k_0	-1.23 ± 0.02	-1.39 ± 0.02	-1.48 ± 0.03	-1.58 ± 0.04	-1.48 ± 0.06
Break scale ^b	110^{11}_7	87^8_4	81^9_5	77^{13}_6	90^{29}_{29}
80'' to 180'' (2.91–6.54 kpc)					
Threshold ^a	0.108	0.162	0.216	0.324	none
Number of scans	49	143	225	372	680
Low k/k_0	-0.77 ± 0.04	-0.71 ± 0.03	-0.75 ± 0.03	-0.74 ± 0.03	-0.55 ± 0.03
High k/k_0	-1.10 ± 0.02	-1.28 ± 0.01	-1.35 ± 0.02	-1.44 ± 0.02	-1.50 ± 0.04
Break scale ^b	218^{42}_{26}	192^{54}_{25}	171^{34}_{17}	171^{34}_{15}	173^{41}_{13}

Notes.

^a Peak intensity threshold in units of $10^{-13} \text{ erg s}^{-1} \text{ cm}^{-2} \text{ arcsec}^{-2}$.

^b Break scales are from the intersection points of the power-law fits to the PS on scales larger and smaller than characteristic values of ~ 20 pc, ~ 80 pc, and ~ 150 pc, in order of increasing galactocentric radii. The slopes of the PS are from fits at k/k_0 smaller than and larger than the averages of the fitted break scales, which are taken to be 25 pc, 90 pc, and 180 pc, respectively.

Table 3
PS Results for Pa α at Various Peak Intensity Thresholds

Threshold ^a	0.38	0.51	0.64	1.0	2.0
Number of scans	43	69	89	111	134
Slope, low k/k_0	-0.61 ± 0.07	-0.64 ± 0.07	-0.65 ± 0.07	-0.70 ± 0.08	-0.64 ± 0.08
Slope, high k/k_0	-0.83 ± 0.02	-0.92 ± 0.02	-0.98 ± 0.02	-1.02 ± 0.03	-1.00 ± 0.03
Break scale ^b	168^{81}_{42}	195^{76}_{40}	183^{66}_{34}	121^{46}_{25}	113^{45}_{22}

Notes.

^a Peak intensity threshold in units of $10^{-13} \text{ erg s}^{-1} \text{ cm}^{-2} \text{ arcsec}^{-2}$.

^b Break scales are from the intersection points of the power-law fits to the PS on scales larger and smaller than a characteristic value of ~ 200 pc. The slopes of the PS are from fits at k/k_0 smaller than and larger than the average of the fitted break scale, which is ~ 170 pc.

four circles at 300 pixel, or 100 scan, intervals. All of the intensity scans were complete circles that fit inside the image, so the spatial coverage in Pa α is less than in H α .

PS and PS slopes are shown in the middle of Figure 4. As for H α , the curves from top to bottom are for scans with increasing limits to the peak intensity (see Table 3). A slight break in the PS at ~ 170 pc is evident (vertical black line), but it is more subtle than for H α . The horizontal lines in the bottom panel show PS slopes for k/k_0 smaller and larger than the value at 170 pc, again extending to 5 times the FWHM.

Compared to H α , Pa α has lower signal-to-noise for the same physical regions. For Case B recombination, the Pa α intensity should be one-eighth of the H α intensity. The lowest threshold for Pa α emission in Table 3, for which there are 43 scans, is $0.38 \times 10^{-14} \text{ erg s}^{-1} \text{ cm}^{-2} \text{ arcsec}^{-2}$. The equivalent emission measure in H α has an intensity 8 times larger, or 3.04×10^{-14} in the same units, which is comparable to the highest H α threshold in Table 1, with 710 scans.

5. Power Spectra for Broadband Mid-infrared Emission

Images of M51 from JWST in eight mid-infrared passbands were examined for evidence of disk thickness in PS. Unlike the H α and Pa α images, which have 0.04 pixels and FWHM PSF resolutions of 0.07, the broadband images have 0.11 pixels and various resolutions, depending on the wavelength. The (filter, FWHM resolution) combinations for the MIRI images are: (F560W, 0.207), (F770W, 0.269), (F1000W, 0.328), (F1130W, 0.375), (F1280W, 0.420), (F1500W, 0.488), (F1800W, 0.591), and (F2100W, 0.674), from the JWST User Documentation.³⁸ Figure 7 shows six circles representing the locations of azimuthal intensity scans separated by 20 scans (equal to 60 pixels) and superposed on the F1130W image.

The right-hand side of Figure 4 shows the PS and their derivatives. Each curve is for a different wavelength through the indicated sequence of JWST filters from top to bottom: F560W, F770W, F1000W, F1130W, F1280W, F1500W, F1800W, and F2100W. The increasing breadth of the dip at high $\log k/k_0$ shows the effect of larger PSFs. In all cases, only scans with low peak intensities were used, as summarized in Table 4.

The broadband PS have a more gradual slope change than H α or Pa α . Nevertheless, we measure the average slopes below and above the wavenumber at 100 pc (the vertical line) for comparison. The threshold intensities, number of scans in each PS, and slopes at low and high $\log k/k_0$, are in Table 4. The longest two mid-infrared wavelengths have no k/k_0 values below 5 times the FWHM of the PSF.

³⁸ <https://jwst-docs.stsci.edu/jwst-mid-infrared-instrument/miri-performance/miri-point-spread-functions>

6. Discussion

6.1. Power Spectrum Breaks and Slopes

Average PS for H α between 1.27 kpc and 7.09 kpc radius, and Pa α between 1.27 kpc and 1.89 kpc radius, show a change in slope at a scale of ~ 120 pc and ~ 170 pc, respectively. The scale for H α increases with radius, from ~ 25 pc at 0.5–1 kpc radius, to ~ 90 pc at 1.27–2.91 kpc, to ~ 180 pc at 2.91–6.54 kpc. These slope changes suggest a transition from two-dimensional to three-dimensional turbulence on these scales, in which case they represent a measure of disk thickness. The radial increase in thickness is consistent with measurements in other galaxies (e.g., K. Yim et al. 2014).

The conversion between length $1/k$ and disk thickness has not been calibrated from observations, but a discussion in F. Bournaud et al. (2010) gives some insight. They simulate an LMC-size galaxy in a 26 kpc box with a midplane resolution less than 13 pc. The average gas disk inside a radius of 5 kpc was fitted to the isothermal equilibrium function, $\text{sech}^2(z/h)$, to obtain $h = 207$ pc. We note that a Gaussian approximation to $\text{sech}^2(z/h)$ for small z/h has a dispersion of $h/\sqrt{2}$, and an exponential approximation to this function at large z/h has a scale height of $h/2$. The HWHM where $\text{sech}^2(z/h) = 0.5$ is at $z = 0.88h$. Also in this simulation, the PS of the surface density viewed perpendicular to the disk had a break at $k_{\text{br}} \sim 100$, which corresponds to $(13,000 \text{ pc})/(2\pi k_{\text{br}}) = 21.3$ pc. The authors consider a measure of thickness to be $2\pi/k_{\text{br}}$, which would be 134 pc.

F. Combes et al. (2012) measured PS breaks in M33 and in corresponding simulations. For the simulations, they compared the scale of the PS break ($1/k_{\text{br}}$) and the thickness measured as $H_z = 2.35(\langle z^2 \rangle - \langle z \rangle^2)^{1/2}$, which is the FWHM for a Gaussian. They found that $k_{\text{br}}H_z$ varies between 0.24 and 1.07 with an average of 0.66 among nine simulations, depending on the details of the feedback that contributes to turbulence on various scales.

A. Lazarian & D. Pogosyan (2000) determine PS for turbulent emissions when there are bulk velocity gradients along the line of sight, as in Milky Way observations along the galactic plane. They define a characteristic scale as the length (λ in their notation) where the line-of-sight turbulent speed equals the change in bulk velocity. PS show a break at $\lambda k_{\text{br}} \sim 1$ for observed transverse wavenumber k_{br} . This interpretation of PS breaks is more related to the scale dependence of turbulent speed than our interpretation, which is a measure of line-of-sight thickness in another galaxy.

Our results may be compared with measurements by J. Pety et al. (2013) of the thick component of CO in M51, which was inferred to have a scale height of 190–250 pc using combined information from radio interferometry and a single dish

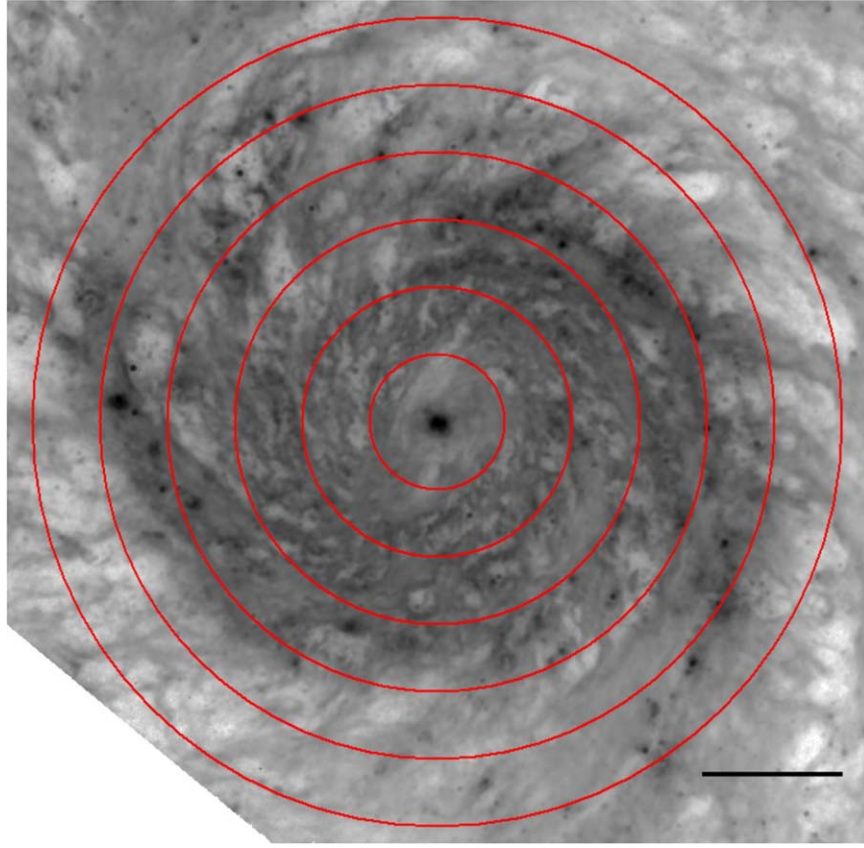


Figure 7. Image of M51 in the F1130W filter with circles at the positions of sample intensity scans spaced by 60 pixels, which corresponds to 20 scans, 6.6, or 240 pc. The image is plotted as log of the intensity. The scale bar is 500 pc.

Table 4
PS Results for Broadband Mid-infrared Images

	JWST Filter			
	F560W	F770W	F1000W	F1130
Threshold ^a	20	95	35	110
Number of scans	26	26	33	33
Slope, low k/k_0	-0.95 ± 0.09	-0.74 ± 0.08	-0.92 ± 0.06	-0.80 ± 0.06
Slope, high k/k_0	-1.40 ± 0.21	-2.13 ± 0.42	-1.72 ± 0.24	-1.91 ± 0.55
Break scale ^b	$25.8^{8.7}_{4.6}$	$31.8^{14}_{3.8}$	$31.0^{7.3}_{3.3}$	$36.3^{11}_{3.8}$

	JWST Filter			
	F1280W	F1500W	F1800W	F2100W
Threshold ^a	90	65	100	130
Number of scans	33	32	30	35
Slope, low k/k_0	-0.78 ± 0.07	-0.88 ± 0.07	-0.91 ± 0.06	-0.93 ± 0.07
Slope, high k/k_0	-1.87 ± 1.39	-1.58 ± 5.20
Break scale ^b	$34.7^{12}_{4.0}$	$35.4^{10.4}_{4.7}$

Notes.

^a Peak intensity threshold in units of megajanskys per steradian.

^b The slopes of the PS are from fits at k/k_0 smaller than and larger than a fiducial break scale of 100 pc. The tabulated break scales are from the intersection points of the resulting power-law fits. There are no evident breaks in the broadband PS, so these scales are not considered to be measures of disk thickness.

telescope. Our results are also comparable with the 95–178 pc thickness derived by T. Hu et al. (2013) from the spiral arm pitch angle and density wave theory. Our thinner measurements for H α at intermediate radii are consistent with the 40 pc scale height (80 pc thickness) for the thin component of CO in J. Pety et al. (2013) and also with the molecular disk thickness of 80 pc in the simulation of M51 by R. G. Tress et al. (2020).

J. Pety et al. (2013) derive a scale height of 10–20 pc in the inner kpc for their thin component, which is consistent with our ≤ 25 pc measurement inside 35'' (1.27 kpc). Considering this, our measurement of the length scale at the break, which in our notation is $2/(k/k_0)_{\text{br}}$ multiplied by the pixel size in parsecs (i.e., 1.45 pc for H α), should be directly comparable to the scale height or half-thickness of the disk.

The increase in inverse break wavenumber with galactocentric radius, R , measured here for M51 corresponds to approximately 40 pc per kpc in radius, starting from ~ 0 pc thickness at the center; i.e., $k_{\text{br}}(\text{pc})^{-1} \sim 40R(\text{kpc})$. This was determined from the $180-25 = 155$ pc scale increase over a radial range from 0.75 kpc to $0.5 \times (2.91 + 6.54) = 4.7$ kpc. This rate of increase for $\text{H}\alpha$ is ~ 4 – 6 times faster than for various gas components in the edge-on galaxy NGC 891, where the scale heights have been directly measured to be $H(\text{pc}) = (120 \pm 1) + (8.3 \pm 0.1)R(\text{kpc})$ for CO, $H(\text{pc}) = (151 \pm 5) + (11.6 \pm 0.5)R(\text{kpc})$ for H I (K. Yim et al. 2014), and $H(\text{pc}) = (49.9 \pm 32.9) \pm (6.3 \pm 3.1)R(\text{kpc})$ for bright $8 \mu\text{m}$ sources associated with star formation (B. G. Elmegreen & D. M. Elmegreen 2020). However, the rate of increase for M51 is comparable to that for more face-on spirals in P. E. Mancera Piña et al. (2022), where the thicknesses were determined from hydrostatic equilibrium.

The fast rate of thickness increase in M51 could be related to its recent interaction with NGC 5195. Strong interactions have been found to increase the gas velocity dispersion by a factor of ~ 2 or more in both observations (B. G. Elmegreen et al. 1993; J. A. Irwin 1994; M. Kaufman et al. 1997, 1999; I. Goldman 2000; T. Ashley et al. 2013) and simulations (B. Burkhardt et al. 2010; F. Renaud et al. 2014). For a minor interaction like NGC 5195 with M51, only the outer regions may be affected (F. Bournaud et al. 2009). Because the disk thickness scales with the square of the velocity dispersion for a given surface density, the interaction could have thickened the outer parts of M51 most, increasing the rate of thickening compared to other galaxies.

The break in the PS observed here shows up most clearly for intensity scans that contain no bright point-like sources. This differs from H I studies of nearby galaxies (LMC, M33; see Section 1), which show a break for PS averaged over large sections of the disk. We could not do the equivalent two-dimensional PS or large-area averaging here because we had to avoid bright sources (trials of this type produced no breaks). The extremes of intensity for $\text{H}\alpha$, $\text{Pa}\alpha$, and MIRI passbands are much larger than for H I, and intensity scans with bright point-like sources have flat PS.

For $\text{H}\alpha$, the PS slopes at low and high k/k_0 average -0.75 ± 0.03 and -1.28 ± 0.07 , respectively, for the first four entries in Table 1. The slopes for $\text{H}\alpha$ at 0.5–1 kpc radius average -0.95 ± 0.04 and -2.43 ± 0.26 , at 1.27–2.91 kpc they average -0.82 ± 0.05 and -1.42 ± 0.13 , and at 2.91–6.54 kpc, they average -0.74 ± 0.04 and -1.29 ± 0.13 . $\text{Pa}\alpha$ slopes average -0.65 ± 0.08 and -0.94 ± 0.08 at low and high k/k_0 for the first four entries in Table 3. For the broadband filters, the average slope at low k/k_0 is -0.86 ± 0.10 and at high k/k_0 it is -1.77 ± 0.23 .

These low- k/k_0 slopes are all similar, averaging -0.80 ± 0.10 , but the high k/k_0 slopes have considerable variation, averaging -1.52 ± 0.47 . $\text{Pa}\alpha$ differs from $\text{H}\alpha$ because the difference in slopes between low and high k/k_0 is smaller for $\text{Pa}\alpha$, making the presence of a break in $\text{Pa}\alpha$ more uncertain. The slope difference at mid-infrared wavelengths from the MIRI observations is larger than for either $\text{H}\alpha$ or $\text{Pa}\alpha$, but the high- k/k_0 slope is possibly contaminated by the steep decline of the PS into the PSF.

6.2. $\text{H}\alpha$ Intensities

The low-intensity emission observed in $\text{H}\alpha$ is brighter than the DIG in the Milky Way (R. J. Reynolds 2004). The intensity

values in Figure 2 and our threshold values in Table 1 correspond to an intensity of $\sim 10^{-14} \text{ erg s}^{-1} \text{ cm}^{-2} \text{ arcsec}^{-2}$. R. J. Reynolds (1992) observed the local DIG with an intensity $I \sin(b) \sim 2.9 \times 10^{-7} \text{ erg s}^{-1} \text{ cm}^{-2} \text{ sr}^{-1}$ for galactic latitude b , which is, after multiplying by 2 for the whole disk and converting to our units, $1.4 \times 10^{-17} \text{ erg s}^{-1} \text{ cm}^{-2} \text{ arcsec}^{-2}$. This is 10^{-3} times fainter than the weak emission in M51 and fainter than our 1σ noise level. Although the star formation rate per unit area in M51 is larger than it is locally, the additional star formation is not enough to explain the M51 emission as equivalent to Milky Way DIG.

We may get some insight into the origin of the M51 $\text{H}\alpha$ by converting the intensity to an emission measure. From R. J. Reynolds (1992), the $\text{H}\alpha$ intensity I and emission measure, EM, for case B recombination (where Lyman emission lines are absorbed locally) are related by

$$I = 2.0 \times 10^{-18} T_4^{-0.92} \text{ EM erg s}^{-1} \text{ cm}^{-2} \text{ arcsec}^{-2}, \quad (1)$$

where EM is $n_e^2 L$ for electron density n_e in cubic centimeters and path length L in parsecs. Here, we have converted steradians to arcsec². Setting $T_4 = 0.8$ (R. J. Reynolds 1992), and $I = 10^{-14} \text{ erg s}^{-1} \text{ cm}^{-2} \text{ arcsec}^{-2}$ for the faint component used in our average PS, we obtain $\text{EM} = 4.0 \times 10^3 \text{ cm}^{-6} \text{ pc}$. If we use the inferred disk thickness of $L \sim 100 \text{ pc}$, then $n_e = 6.3 \text{ cm}^{-3}$. This electron density is much higher than in the DIG of the Milky Way, where $n_e \sim 0.1 \text{ cm}^{-3}$.

Slit spectra measurements by C. G. Hoopes & R. A. M. Walterbos (2003) of the DIG in M51 obtained $\text{EM} \sim 30 \text{ cm}^{-6} \text{ pc}$ in the interarm regions, $\sim 50 \text{ cm}^{-6} \text{ pc}$ in the arms and $\sim 200 \text{ cm}^{-6} \text{ pc}$ in a few H II regions. These correspond to $\text{H}\alpha$ intensities of 7.5, 12.6, and 50.3 in units of $10^{-17} \text{ erg s}^{-1} \text{ cm}^{-2} \text{ arcsec}^{-2}$, which are comparable to or slightly greater than our 3σ limit of $7.7 \times 10^{-17} \text{ erg s}^{-1} \text{ cm}^{-2} \text{ arcsec}^{-2}$. The M51 DIG is essentially at our noise limit.

The higher emission that dominates our PS are probably from numerous low-mass star-forming regions, while the DIG is some underlying component that does not contribute much to the PS. The average density in the thin molecular component detected by J. Pety et al. (2013) is $\sim 10 \text{ cm}^{-3}$ at mid-disk, and higher by a factor of ~ 4 at 1 kpc. This molecular component exceeds the density of atomic hydrogen by a factor of ~ 26 at 1 kpc (J. Pety et al. 2013). Ionized gas at this density would explain our average $\text{H}\alpha$ intensity. The presence and even dominance of such dense gas in ionized and molecular form suggest very different interstellar media in the Milky Way and M51, making it conceivable that there is a change from discrete and separate H II regions in a Milky Way-type galaxy to overlapping H II regions in M51.

Some of the $\text{H}\alpha$ emission from M51 could come from scattering off dust. J. E. Barnes et al. (2015) show from MHD simulations and fractal models that most of the scattering occurs near the midplane near the brightest H II regions, but 5%–10% can come from a height of 300 pc. For a face-on view, less than 10%–20% of the $\text{H}\alpha$ is scattered, although the scattering fraction off the surfaces of dense, high latitude clouds could be $\sim 40\%$.

Our previous observations of four other galaxies in several of the mid-infrared JWST bands used here, including the spirals NGC 628 and NGC 5236, also showed no break in the PS, even when considering the faintest emission (Paper I). We suggested that the disks emitting in these passbands are too thin for the

spatial resolution. The same could be true for the MIRI passbands here.

7. Conclusions

The PS of H α emission from M51 has a sudden change of slope at a scale of ~ 120 pc over the main part of the disk, with a range in these scales from ~ 25 pc in the central kpc to ~ 90 pc at ~ 2 kpc and ~ 180 pc at 5 kpc. These slope changes are interpreted as measures of the line-of-sight disk thickness. A less certain measurement at Pa α gives a thickness of ~ 170 pc over a radial range of ~ 1.3 kpc to ~ 1.9 kpc.

The characteristic intensity of H α emission corresponds to an emission measure of $4.0 \times 10^3 \text{ cm}^{-6} \text{ pc}$, and, for a line-of-sight thickness of 100 pc, an electron density of 6.4 cm^{-3} . This emission measure is nearly 2 orders of magnitude higher than the DIG emission measure in the Milky Way and M51, which emphasizes that our PS are dominated by star-forming regions.

Broadband emission in the JWST MIRI filters did not indicate a particular length scale in the PS, although the slope clearly changes from large scales to small. Part of the difference with the other observations is that the PSF is broad at these mid-infrared wavelengths. In addition, the mid-infrared emission from dust could trace a thinner component of the gas.

Acknowledgments




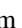





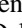
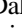
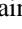



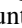

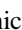

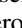


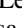


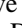
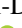

Helpful comments by Dr. Alex Lazarian and the referee, Dr. Frederic Bournaud, are appreciated. This work is based on observations made with the NASA/ESA/CSA James Webb Space Telescope and retrieved from the Mikulski Archive for Space Telescopes at the Space Telescope Science Institute, which is operated by the Association of Universities for Research in Astronomy, Inc., under NASA contract NAS 5-03127. These observations are associated with GO programs #1783 and #3435. The work also made use of archival data from the NASA/ESA Hubble Space Telescope obtained from the Space Telescope Science Institute, which is operated by the Association of Universities for Research in Astronomy, Inc., under NASA contract NAS 5-26555. Data presented in this article were obtained from the Mikulski Archive for Space Telescopes (MAST) at the Space Telescope Science Institute. The specific observations analyzed can be accessed via DOI: [10.17909/jp5q-s259](https://doi.org/10.17909/jp5q-s259) (Dataset Title: M51/Elmegreen/Calzetti). Support for programs GO #1783 and GO #3435 was provided by NASA through grants from the Space Telescope Science Institute. V.J., J.G., and B.G. acknowledge support from grant JWST-GO-01783; K.S., D.D., M.L.B., D.C., A.K.L., and J.D.S. acknowledge support from grant JWST-GO-03435. A. A. acknowledges support from the Swedish National Space Agency (SNSA) through grant 2021-00108. R.S.K. acknowledges financial support from the European Research Council via the ERC Synergy Grant “ECOGAL” (project ID 855130), from the German Excellence Strategy via the Heidelberg Cluster of Excellence (EXC 2181 – 390900948) “STRUCTURES,” and from the German Ministry for Economic Affairs and Climate Action in project “MAINN” (funding ID 50002206). R.S.K. also thanks the 2024/25 Class of Radcliffe Fellows for their company and for highly interesting and stimulating discussions. K.G. is supported by the Australian Research Council through the Discovery Early Career Researcher Award (DECRA) Fellowship (project number DE220100766) funded by the Australian Government.

A.D.C. acknowledges the support from the Royal Society University Research Fellowship URF/R1/191609. B.G. is supported by the German Research Foundation (DFG) in the form of an Emmy Noether Research Group – DFG project #542802847 (GA 3170/3-1). The Flatiron Institute is funded by the Simons Foundation.

Facilities: HST, JWST (NIRCam, MIRI).

Software: JWST Calibration Pipeline (H. Bushouse et al. 2022; P. Greenfield & T. Miller 2016); SAOImage DS9 (W. A. Joye & E. Mandel 2003); FORTRAN, VossPlot (R. Voss 1995).

ORCID iDs

Bruce G. Elmegreen  <https://orcid.org/0000-0002-1723-6330>
 Daniela Calzetti  <https://orcid.org/0000-0002-5189-8004>
 Angela Adamo  <https://orcid.org/0000-0002-8192-8091>
 Karin Sandstrom  <https://orcid.org/0000-0002-4378-8534>
 Daniel Dale  <https://orcid.org/0000-0002-5782-9093>
 Varun Bajaj  <https://orcid.org/0009-0008-4009-3391>
 Martha L. Boyer  <https://orcid.org/0000-0003-4850-9589>
 Ana Duarte-Cabral  <https://orcid.org/0000-0002-5259-4774>
 Ryan Chown  <https://orcid.org/0000-0001-8241-7704>
 Matteo Correnti  <https://orcid.org/0000-0001-6464-3257>
 Julianne J. Dalcanton  <https://orcid.org/0000-0002-1264-2006>
 Bruce T. Draine  <https://orcid.org/0000-0002-0846-936X>
 Brandt Gaches  <https://orcid.org/0000-0003-4224-6829>
 John S. Gallagher, III  <https://orcid.org/0000-0001-8608-0408>
 Kathryn Grasha  <https://orcid.org/0000-0002-3247-5321>
 Benjamin Gregg  <https://orcid.org/0000-0003-4910-8939>
 Leslie K. Hunt  <https://orcid.org/0000-0001-9162-2371>
 Kelsey E. Johnson  <https://orcid.org/0000-0001-8348-2671>
 Robert Kennicutt, Jr.  <https://orcid.org/0000-0001-5448-1821>
 Ralf S. Klessen  <https://orcid.org/0000-0002-0560-3172>
 Adam K. Leroy  <https://orcid.org/0000-0002-2545-1700>
 Sean Linden  <https://orcid.org/0000-0002-1000-6081>
 Anna F. McLeod  <https://orcid.org/0000-0002-5456-523X>
 Matteo Messa  <https://orcid.org/0000-0003-1427-2456>
 Göran Östlin  <https://orcid.org/0000-0002-3005-1349>
 Mansi Padave  <https://orcid.org/0000-0002-3472-0490>
 Julia Roman-Duval  <https://orcid.org/0000-0001-6326-7069>
 J. D. Smith  <https://orcid.org/0000-0003-1545-5078>
 Fabian Walter  <https://orcid.org/0000-0003-4793-7880>
 Tony D. Weinbeck  <https://orcid.org/0009-0005-8923-558X>

References

- Armstrong, J. W., Rickett, B. J., & Spangler, S. R. 1995, *ApJ*, **443**, 209
- Ashley, T., Simpson, C. E., & Elmegreen, B. G. 2013, *AJ*, **146**, 42
- Bacchini, C., Fraternali, F., Iorio, G., & Pezzulli, G. 2019, *A&A*, **622**, A64
- Bacchini, C., Fraternali, F., Iorio, G., et al. 2020, *A&A*, **641**, A70
- Bagetakos, I., Brinks, E., Walter, F., et al. 2011, *AJ*, **141**, 23
- Banerjee, A., & Jog, C. J. 2008, *ApJ*, **685**, 254
- Banerjee, A., & Jog, C. J. 2011, *ApJL*, **732**, L8
- Banerjee, A., & Jog, C. J. 2013, *MNRAS*, **431**, 582
- Banerjee, A., Jog, C. J., Brinks, E., & Bagetakos, I. 2011, *MNRAS*, **415**, 687
- Banerjee, A., Matthews, L. D., & Jog, C. J. 2010, *NewA*, **15**, 89
- Barnes, J. E., Wood, K., Hill, A. S., & Haffner, L. M. 2015, *MNRAS*, **447**, 559
- Block, D. L., Puerari, I., Elmegreen, B. G., & Bournaud, F. 2010, *ApJL*, **718**, L1
- Bournaud, F., Elmegreen, B. G., & Martig, M. 2009, *ApJL*, **707**, L1
- Bournaud, F., Elmegreen, B. G., Teyssier, R., Block, D. L., & Puerari, I. 2010, *MNRAS*, **409**, 1088
- Burkhart, B., Stanimirović, S., Lazarian, A., & Kowal, G. 2010, *ApJ*, **708**, 1204
- Bushouse, H., Eisenhamer, J., Dencheva, N., et al. 2022, JWST Calibration Pipeline, v1.9.0, Zenodo, doi:[10.5281/zenodo.7487203](https://doi.org/10.5281/zenodo.7487203)
- Calzetti, D., Adamo, A., Linden, S. T., et al. 2024, *ApJ*, **971**, 118
- Combes, F., Boquien, M., Kramer, C., et al. 2012, *A&A*, **539**, A67

- Crovisier, J., & Dickey, J. M. 1983, *A&A*, **122**, 282
- Csörnyei, G., Anderson, R. I., Vogl, C., et al. 2023, *A&A*, **678**, A44
- Dettmar, R. J. 1990, *A&A*, **232**, L15
- Dutta, P., Begum, A., Bharadwaj, S., & Chengalur, J. N. 2009, *MNRAS*, **397**, L60
- Dutta, P., Begum, A., Bharadwaj, S., & Chengalur, J. N. 2010, *MNRAS*, **405**, L102
- Dutta, P., Begum, A., Bharadwaj, S., & Chengalur, J. N. 2013, *NewA*, **19**, 89
- Elmegreen, B. G., Adamo, A., Baja, V., et al. 2025, *OJAp*, **8**, 21
- Elmegreen, B. G., & Elmegreen, D. M. 2020, *ApJ*, **895**, 71
- Elmegreen, B. G., Elmegreen, D. M., & Leitner, S. N. 2003, *ApJ*, **590**, 271
- Elmegreen, B. G., & Hunter, D. A. 2015, *ApJ*, **805**, 145
- Elmegreen, B. G., Kaufman, M., & Thomasson, M. 1993, *ApJ*, **412**, 90
- Elmegreen, B. G., Kim, S., & Staveley-Smith, L. 2001, *ApJ*, **548**, 749
- Elmegreen, B. G., & Scalo, J. 2004, *ARA&A*, **42**, 211
- Fensch, J., Bournaud, F., Brucy, N., et al. 2023, *A&A*, **672**, A193
- García-Burillo, S., Guelin, M., Cernicharo, J., & Dahlem, M. 1992, *A&A*, **266**, 21
- Girichidis, P., Walch, S., Naab, T., et al. 2016, *MNRAS*, **456**, 3432
- Goldman, I. 2000, *ApJ*, **541**, 701
- Greenfield, P., & Miller, T. 2016, *A&C*, **16**, 41
- Gregg, B., Calzetti, D., Adamo, A., et al. 2024, *ApJ*, **971**, 115
- Grisdale, K., Agertz, O., Romeo, A. B., Renaud, F., & Read, J. I. 2017, *MNRAS*, **466**, 1093
- Heyer, M., & Dame, T. M. 2015, *ARA&A*, **53**, 583
- Hill, A. S., Mac Low, M.-M., Gatto, A., & Ibáñez-Mejía, J. C. 2018, *ApJ*, **862**, 55
- Hoopes, C. G., & Walterbos, R. A. M. 2003, *ApJ*, **586**, 902
- Howk, J. C., & Savage, B. D. 2000, *AJ*, **119**, 644
- Hu, T., Shao, Z., & Peng, Q. 2013, *ApJL*, **762**, L27
- Irwin, J. A. 1994, *ApJ*, **429**, 618
- Jeffreson, S. M. R., Sun, J., & Wilson, C. D. 2022, *MNRAS*, **515**, 1663
- Joye, W. A., & Mandel, E. 2003, in ASP Conf. Ser. 295, *Astronomical Data Analysis Software and Systems XII*, ed. H. E. Payne, R. I. Jedrzejewski, & R. N. Hook (San Francisco, CA: ASP), 489
- Kalberla, P. M. W., Dedes, L., Kerp, J., & Haud, U. 2007, *A&A*, **469**, 511
- Kaufman, M., Brinks, E., Elmegreen, B. G., et al. 1999, *AJ*, **118**, 1577
- Kaufman, M., Brinks, E., Elmegreen, D. M., et al. 1997, *AJ*, **114**, 2323
- Koch, E. W., Chiang, I.-D., Utomo, D., et al. 2020, *MNRAS*, **492**, 2663
- Koyama, H., & Ostriker, E. C. 2009, *ApJ*, **693**, 1346
- Lazarian, A., & Pogosyan, D. 2000, *ApJ*, **537**, 720
- Li, X., Shi, Y., Zhang, Z.-Y., et al. 2022, *MNRAS*, **516**, 4220
- Mancera Piña, P. E., Fraternali, F., Oosterloo, T., et al. 2022, *MNRAS*, **514**, 3329
- Matthews, L. D., & Uson, J. M. 2008, *AJ*, **135**, 291
- Messa, M., Calzetti, D., Adamo, A., et al. 2021, *ApJ*, **909**, 121
- Molina, J., Ibar, E., Godoy, N., et al. 2020, *A&A*, **643**, A78
- Nandakumar, M., & Dutta, P. 2023, *MNRAS*, **526**, 4690
- Narayan, C. A., & Jog, C. J. 2002, *A&A*, **394**, 89
- Ostriker, E. C., McKee, C. F., & Leroy, A. K. 2010, *ApJ*, **721**, 975
- Parker, E. N. 1966, *ApJ*, **145**, 811
- Patra, N. N. 2018, *MNRAS*, **478**, 4931
- Patra, N. N. 2019, *MNRAS*, **484**, 81
- Patra, N. N. 2020a, *MNRAS*, **495**, 2867
- Patra, N. N. 2020b, *MNRAS*, **499**, 2063
- Patra, N. N. 2021, *MNRAS*, **501**, 3527
- Patra, N. N., Banerjee, A., Chengalur, J. N., & Begum, A. 2014, *MNRAS*, **445**, 1424
- Peng, Q.-H. 1988, *A&A*, **206**, 18
- Pety, J., Schinnerer, E., Leroy, A. K., et al. 2013, *ApJ*, **779**, 43
- Rand, R. J., Kulkarni, S. R., & Hester, J. J. 1990, *ApJL*, **352**, L1
- Randriamampandry, T. H., Wang, J., & Mogotsi, K. M. 2021, *ApJ*, **916**, 26
- Renaud, F., Bournaud, F., Kraljic, K., & Duc, P. A. 2014, *MNRAS*, **442**, L33
- Reynolds, R. J. 1992, *ApJL*, **392**, L35
- Reynolds, R. J. 2004, *AdSpR*, **34**, 27
- Roman-Duval, J., Heyer, M., Brunt, C. M., et al. 2016, *ApJ*, **818**, 144
- Rossa, J., Dettmar, R.-J., Walterbos, R. A. M., & Norman, C. A. 2004, *AJ*, **128**, 674
- Sarkar, S., & Jog, C. J. 2018, *A&A*, **617**, A142
- Scoville, N. Z., Thakkar, D., Carlstrom, J. E., & Sargent, A. I. 1993, *ApJL*, **404**, L59
- Spitzer, L., Jr. 1942, *ApJ*, **95**, 329
- Szotkowski, S., Yoder, D., Stanimirović, S., et al. 2019, *ApJ*, **887**, 111
- Tamburro, D., Rix, H. W., Leroy, A. K., et al. 2009, *AJ*, **137**, 4424
- Tress, R. G., Smith, R. J., Sormani, M. C., et al. 2020, *MNRAS*, **492**, 2973
- van der Kruit, P. C. 1981, *A&A*, **99**, 298
- Verbeke, R., Papastergis, E., Ponomareva, A. A., Rathi, S., & De Rijcke, S. 2017, *A&A*, **607**, A13
- Voss, R. 1995, *VossPlot: A Software Tool for Scientific and Technical Graphics* (Berlin: Springer)
- Wilson, C. D., Elmegreen, B. G., Bemis, A., & Brunetti, N. 2019, *ApJ*, **882**, 5
- Yim, K., Wong, T., Howk, J. C., & van der Hulst, J. M. 2011, *AJ*, **141**, 48
- Yim, K., Wong, T., Xue, R., et al. 2014, *AJ*, **148**, 127